Design and Analysis of Low-Distortion Demodulators for Modulated Sensors

Steven Ian Moore [ID], Michael G. Ruppert [ID], *Member, IEEE*, David M. Harcombe, Andrew J. Fleming [ID], *Member, IEEE*, and Yuen Kuan Yong [ID], *Member, IEEE*

Abstract—**System-based demodulators in the form of a Kalman and Lyapunov filter have been demonstrated to significantly outperform traditional demodulators, such as the lock-in amplifier, in bandwidth sensitive applications, for example, high-speed atomic force microscopy. Building on their closed-loop architecture, this paper describes a broader class of high-speed closed-loop demodulators. The generic structure provides greater flexibility to independently control the bandwidth and sensitivity to out-of-band frequencies. A linear time invariant description is derived, which allows the utilization of linear control theory to design the demodulator. Experimental results on a nanopositioner with capacitive sensors demonstrate that the realization of arbitrary demodulator dynamics while achieving excellent noise rejection.**

Index Terms—**Amplitude estimation, demodulation, frequency estimation, phase estimation, transducers.**

I. INTRODUCTION

DEMODULATION is typically a slow process requiring the measurement of a signal over many cycles to accurately extract amplitude, phase, and frequency information. The low measurement bandwidth is detrimental for applications, such as electrostatic [1] and electrothermal [2] MEMS sensing, capacitive tomography [3], inductive displacement sensing [4], [5], precision position control [6] using capacitive sensors [7], and dynamic mode atomic force microscopy [8]. For the latter, the lock-in amplifier [9] has been adopted as the standard demodulation principle [10]. However, this method generates frequency components in the output signals at plus/minus twice the carrier frequency. These frequency components, denoted image signals in this paper, are distortions in the amplitude, phase, and frequency measurements and must be removed by low-pass filtering, thereby limiting the demodulation bandwidth. To alleviate the bandwidth limitation, a number of

high-speed demodulator designs have been reported [11]–[19]. These demodulation techniques are surveyed and compared in [10].

In order to reject the image signal without filtering, the high-bandwidth lock-in amplifier [15] employs an all-pass filter to phase shift the input signal by 90° at the carrier frequency in order to perform image rejection. In another method, the numerical integration performed by FIR filters in the digital lock-in amplifier [14] naturally generates zeros at the harmonics of the carrier frequency to reject the image signal [10]. In both cases, the dependency between carrier frequency and the filter parameters limits the robustness of the demodulators for fast changing input signals and the filters require retuning for a change in carrier frequency.

In contrast, system-based demodulators in the form of a Kalman filter [16], [17] and Lyapunov filter [18], [19] have demonstrated amplitude and phase estimation at high bandwidths without the image signal. However, due to the first-order response of the present system-based demodulators, the resulting frequency responses have a fixed 20 dB/decade attenuation, thus disturbance frequency components are not significantly rejected and can distort the measurement signal. The parameters used to tune the Kalman and Lyapunov demodulator allow only bandwidth to be specified and not stop-band attenuation. While the Lyapunov filter architecture can be generalized to allow for the direct design of higher order demodulators [20], the exact transformation does not allow for arbitrary filter responses.

This paper proposes a demodulator based on a general Lyapunov closed-loop architecture, for which an approximate linear time invariant (LTI) description is derived and presented in Sections III and IV. This approach allows LTI controller design tools to be employed to define the characteristics of the demodulator. Furthermore, models are presented that predict the dynamic response of the proposed demodulators from the in-phase and quadrature states of the input signal to the in-phase and quadrature states of the estimate. These models accurately predict the experimental performance in Section V. Finally, Section VI demonstrates the use of the proposed demodulator in a capacitive sensing application.

II. ARCHITECTURE AND DESIGN FORMULA OF THE PROPOSED DEMODULATOR

The proposed demodulator and the design formula are initially presented for the benefit of practitioners implementing
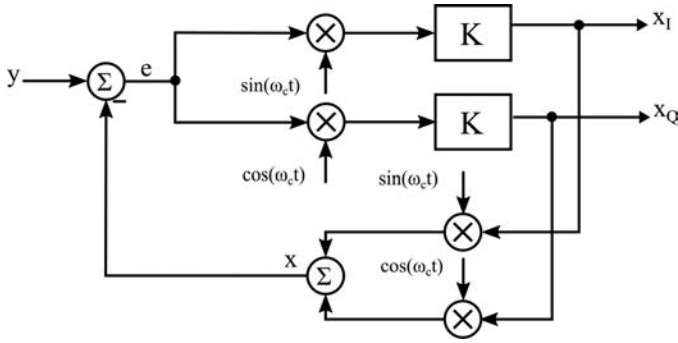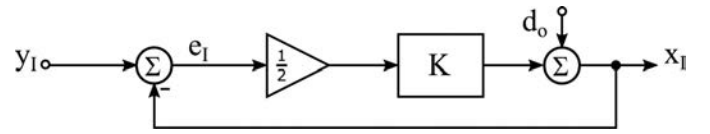
Fig. 1.   Schematic of the demodulator.

Fig. 2.   Block diagram of the linear model of the in-phase half of the demodulator. The output disturbance d_o models the image and cross-coupling signals and linearization errors.

this system. The subsequent Sections III and IV present analysis upon which the design formula is based.

A. Architecture

The demodulator estimates the in-phase and quadrature states of an input sinusoidal signal. The input signal is

$$y(t) = A(t)\sin(\omega_c t + \phi(t)) \tag{1}$$

$$= y_I(t)\sin(\omega_c t) + y_Q(t)\cos(\omega_c t) \tag{2}$$

where $A(t)$ is the amplitude, $\phi(t)$ is the phase, y_I is the in-phase state, y_Q is the quadrature state, and ω_c is the carrier frequency. The characteristic equations that define the demodulator are

$$x_I(t) = K\sin(\omega_c t)(y(t) - x(t)) \tag{3}$$

$$x_Q(t) = K\cos(\omega_c t)(y(t) - x(t)) \tag{4}$$

$$x(t) = x_I(t)\sin(\omega_c t) + x_Q(t)\cos(\omega_c t) \tag{5}$$

where x_I and x_Q are estimates of the states y_I and y_Q, respectively, K is an LTI system, and x is an estimate of the input. Fig. 1 shows a block diagram implementation of the characteristic equations.

This architecture is a derivative of the Kalman filter based demodulator architecture [17] with two modifications. First, the Kalman gains are replaced by the signals $\cos(\omega_c t)$ and $\sin(\omega_c t)$ [see (3) and (4)] as it was demonstrated empirically that the Kalman gains settle to sinusoidal signals with a 90° phase shift between them [17]. Second, the integrations required for the state update in the Kalman filter are replaced with the system K.

The demodulator operates as follows: the difference between the input signal y and its estimate x forms the error signal e. The error signal is mixed with in-phase and quadrature sinusoids and then filtered by the operator K, resulting in the estimated states (x_I, x_Q). Finally, the estimated states are fed back and mixed with in-phase and quadrature sinusoids to form the estimate x. With an appropriate choice of K, the estimated states (x_I, x_Q) converge toward the input states (y_I, y_Q).

From the in-phase and quadrature (IQ) demodulation, estimates for amplitude, phase, and frequency can be obtained

from

$$A = \sqrt{x_I^2 + x_Q^2} \tag{6}$$

$$\phi = \tan^{-1}\left(\frac{x_Q}{x_I}\right) \tag{7}$$

$$\Delta\omega = \frac{d\phi}{dt} \tag{8}$$

where $\Delta\omega$ is the difference between the frequency of the input signal and the carrier frequency [21].

B. Design Formula

The mapping from the input states (y_I, y_Q) to the estimated states (x_I, x_Q) in the Laplace domain can be approximated by the linear model, as shown in Fig. 2. For linearization, the demodulation of the error signal is modeled as a gain of $\frac{1}{2}$ and the mixing-induced image and cross-coupling signals are treated as output disturbances. In the Laplace domain, the linear model is

$$X_I(s) = \frac{K(s)}{2 + K(s)}Y_I(s) = T(s)Y_I(s) \tag{9}$$

$$X_Q(s) = \frac{K(s)}{2 + K(s)}Y_Q(s) = T(s)Y_Q(s) \tag{10}$$

where $T(s)$ is the complementary sensitivity function. $T(s)$ is the design parameter defining the characteristics of the demodulator. It must be stable and have a low-pass frequency response. Then, the transfer function of the system K is computed from

$$K(s) = \frac{2T(s)}{1 - T(s)}. \tag{11}$$

The analysis which justifies the design equation in (11) is provided in Section IV.

C. Selection of $T(s)$

The two design specifications for the demodulator are tracking bandwidth and off-mode rejection as described in [10]. These specifications are parameterized by the transfer function $T(s)$. The tracking bandwidth characterizes the time taken for the estimated states (x_I, x_Q) to converge to the input states (y_I, y_Q) and is specified as the bandwidth of the transfer function $T(s)$.

The off-mode rejection $L(\Delta\omega)$ characterizes the sensitivity to other frequency components and is defined as the ratio in magnitude response at a frequency offset $\Delta\omega$ from the carrier

frequency with respect to the response at the carrier frequency

$$L(\Delta\omega) = \frac{|T(j(\omega_c + \Delta\omega))|}{|T(j\omega_c)|}. \tag{12}$$

III. LAPLACE DOMAIN DESCRIPTION OF THE DEMODULATOR

The exact linear time varying model is important to understand the nuances of the demodulator's performance, and to provide a basis for the LTI approximations used for design. The analysis in this section derives the transfer functions that map the input states $Y_I(s)$ and $Y_Q(s)$ to the estimated states $X_I(s)$ and $X_Q(s)$ in the Laplace domain. A condensed notation is used in this paper to express the frequency shifted versions of the signals and systems that compose the demodulator. For the system K this notation is

$$K_m \equiv K(s + jm\omega_c). \tag{13}$$

This notation is also used for $Y_{I(m)}, Y_{Q(m)}, X_{I(m)}, X_{Q(m)}$. Substituting (2) and (5) into (3) and (4) and applying the Laplace transform leads to the following expressions for $X_{I(0)}$ and $X_{Q(0)}$:

$$X_{I(0)} = \frac{1}{4}K_0 \left[-Y_{I(-2)} + 2Y_{I(0)} - Y_{I(2)} - jY_{Q(-2)} \right.$$
$$\left. + jY_{Q(2)} + X_{I(-2)} - 2X_{I(0)} + X_{I(2)} \right.$$
$$\left. + jX_{Q(-2)} - jX_{Q(2)} \right] \tag{14}$$

$$X_{Q(0)} = \frac{1}{4}K_0 \left[Y_{Q(-2)} + 2Y_{Q(0)} + Y_{Q(2)} - jY_{I(-2)} \right.$$
$$\left. + jY_{I(2)} - X_{Q(-2)} - 2X_{Q(0)} - X_{Q(2)} \right.$$
$$\left. + jX_{I(-2)} - jX_{I(2)} \right]. \tag{15}$$

Solving for $X_{I(0)}$ and $X_{Q(0)}$ results in the equations

$$X_{I(0)} = H_0 \left[-Y_{I(-2)} + 2Y_{I(0)} - Y_{I(2)} - jY_{Q(-2)} \right.$$
$$\left. + jY_{Q(2)} + X_{I(-2)} + X_{I(2)} + jX_{Q(-2)} \right.$$
$$\left. - jX_{Q(2)} \right] \tag{16}$$

$$X_{Q(0)} = H_0 \left[Y_{Q(-2)} + 2Y_{Q(0)} + Y_{Q(2)} - jY_{I(-2)} \right.$$
$$\left. + jY_{I(2)} - X_{Q(-2)} - X_{Q(2)} + jX_{I(-2)} \right.$$
$$\left. - jX_{I(2)} \right] \tag{17}$$

where

$$H_m = \frac{\frac{1}{4}K_m}{1 + \frac{1}{2}K_m}. \tag{18}$$

To proceed with the analysis, (16) and (17) are frequency shifted by $\pm 2\omega_c$

$$X_{I(-2)} = H_{-2} \left[-Y_{I(-4)} + 2Y_{I(-2)} - Y_{I(0)} \right.$$
$$\left. - jY_{Q(-4)} + jY_{Q(0)} + X_{I(-4)} + X_{I(0)} \right.$$
$$\left. + jX_{Q(-4)} - jX_{Q(0)} \right] \tag{19}$$

$$X_{Q(-2)} = H_{-2} \left[Y_{Q(-4)} + 2Y_{Q(-2)} + Y_{Q(0)} - jY_{I(-4)} \right.$$

$$\left. + jY_{I(0)} - X_{Q(-4)} - X_{Q(0)} \right.$$
$$\left. + jX_{I(-4)} - jX_{I(0)} \right] \tag{20}$$

$$X_{I(2)} = H_2 \left[-Y_{I(0)} + 2Y_{I(2)} - Y_{I(4)} - jY_{Q(0)} \right.$$
$$\left. + jY_{Q(4)} + X_{I(0)} + X_{I(4)} + jX_{Q(0)} \right.$$
$$\left. - jX_{Q(4)} \right] \tag{21}$$

$$X_{Q(2)} = H_2 \left[Y_{Q(0)} + 2Y_{Q(2)} + Y_{Q(4)} - jY_{I(0)} \right.$$
$$\left. + jY_{I(4)} - X_{Q(0)} - X_{Q(4)} + jX_{I(0)} \right.$$
$$\left. - jX_{I(4)} \right]. \tag{22}$$

Equations (19)–(22) are substituted into (16) and (17). These substitutions result in the terms $X_{I(-2)}, X_{Q(-2)}, X_{I(2)}, X_{Q(2)}, X_{I(-4)}, X_{Q(-4)}, X_{I(4)},$ and $X_{Q(4)}$ being eliminated resulting in the following expressions:

$$X_{I(0)} = H_0 \left[-Y_{I(-2)} + 2Y_{I(0)} - Y_{I(2)} - jY_{Q(-2)} \right.$$
$$\left. + jY_{Q(2)} + 2H_{-2}(X_{I(0)} - jX_{Q(0)} - Y_{I(0)} \right.$$
$$\left. + Y_{I(-2)} + jY_{Q(0)} + jY_{Q(-2)}) + 2H_2(X_{I(0)} \right.$$
$$\left. + jX_{Q(0)} - Y_{I(0)} + Y_{I(2)} - jY_{Q(0)} - jY_{Q(2)}) \right] \tag{23}$$

$$X_{Q(0)} = H_0 \left[Y_{Q(-2)} + 2Y_{Q(0)} + Y_{Q(2)} - jY_{I(-2)} \right.$$
$$\left. + jY_{I(2)} + 2H_{-2}(X_{Q(0)} + jX_{I(0)} - Y_{Q(0)} \right.$$
$$\left. - Y_{Q(-2)} - jY_{I(0)} + jY_{I(-2)}) + 2H_2(X_{Q(0)} \right.$$
$$\left. - jX_{I(0)} - Y_{Q(0)} - Y_{Q(2)} + jY_{I(0)} - jY_{I(2)}) \right]. \tag{24}$$

Equations (23) and (24) are solved for $X_{I(0)}$ and $X_{Q(0)}$ and (18) is substituted into the result. This produces the input–output transfer functions of the demodulator

$$X_I(s) = -\frac{K_0}{2(K_0 + K_{-2} + 2)}Y_{I(-2)} - \frac{K_0}{2(K_0 + K_2 + 2)}Y_{I(2)}$$
$$+ \frac{K_0(2K_0 + K_{-2} + K_2 + 4)}{2(K_0 + K_{-2} + 2)(K_0 + K_2 + 2)}Y_{I(0)}$$
$$- \frac{jK_0}{2(K_0 + K_{-2} + 2)}Y_{Q(-2)} + \frac{jK_0}{2(K_0 + K_2 + 2)}Y_{Q(2)}$$
$$+ \frac{jK_0(K_{-2} - K_2)}{2(K_0 + K_{-2} + 2)(K_0 + K_2 + 2)}Y_Q(s) \tag{25}$$

$$X_Q(s) = -\frac{jK_0}{2(K_0 + K_{-2} + 2)}Y_{I(-2)} + \frac{jK_0}{2(K_0 + K_2 + 2)}Y_{I(2)}$$
$$- \frac{jK_0(K_{-2} - K_2)}{2(K_0 + K_{-2} + 2)(K_0 + K_2 + 2)}Y_{I(0)}$$
$$+ \frac{K_0}{2(K_0 + K_{-2} + 2)}Y_{Q(-2)} + \frac{K_0}{2(K_0 + K_2 + 2)}Y_{Q(2)}$$
$$+ \frac{K_0(2K_0 + K_{-2} + K_2 + 4)}{2(K_0 + K_{-2} + 2)(K_0 + K_2 + 2)}Y_Q(s). \tag{26}$$

The abovementioned equations show how frequency shifted versions of the input states map to the estimated states. An alternative arrangement of these equations shows how the inputs map onto different frequency-shifted estimated states. These relationships in the Laplace domain are

$$X_I(s + 2j\omega_c) = -T_A(s)Y_I(s) - jT_A(s)Y_Q(s) \tag{27}$$

$$X_I(s) = T_B(s)Y_I(s) + T_C(s)Y_Q(s) \tag{28}$$

$$X_I(s - 2j\omega_c) = -T_D(s)Y_I(s) + jT_D(s)Y_Q(s) \tag{29}$$

$$X_Q(s + 2j\omega_c) = -jT_A(s)Y_I(s) + T_A(s)Y_Q(s) \tag{30}$$

$$X_Q(s) = -T_C(s)Y_I(s) + T_B(s)Y_Q(s) \tag{31}$$

$$X_Q(s - 2j\omega_c) = jT_D(s)Y_I(s) + T_D(s)Y_Q(s). \tag{32}$$

Equations (27) and (30) define the image signals resulting from a frequency upconversion, and (29) and (32) define the image signals resulting from a frequency downconversion. The up-converting transfer function $T_A(s)$, the direct-coupling transfer function $T_B(s)$, the cross-coupling transfer function $T_C(s)$, and the downconverting transfer function $T_D(s)$ are

$$T_A(s) = \frac{K_2}{2(K_2 + K_0 + 2)} \tag{33}$$

$$T_B(s) = \frac{K_0(2K_0 + K_{-2} + K_2 + 4)}{2(K_0 + K_{-2} + 2)(K_0 + K_2 + 2)} \tag{34}$$

$$T_C(s) = \frac{jK_0(K_{-2} - K_2)}{2(K_0 + K_{-2} + 2)(K_0 + K_2 + 2)} \tag{35}$$

$$T_D(s) = \frac{K_{-2}}{2(K_{-2} + K_0 + 2)}. \tag{36}$$

IV. LTI ANALYSIS

This section examines LTI approximations of the exact linear time varying model presented in Section III and the conditions under which they are valid. The LTI approximation in (37) is the design formula presented in Section II.

A. LTI Approximations of the Demodulator

The transfer function K_0 should have a high gain at low frequencies and its magnitude response should roll-off as the frequency increases. A high gain is necessary for the estimated states to converge toward the input states. The roll-off is necessary to suppress artifacts that occur due to the mixing in the demodulator. With these characteristics, there is a region R_1 centered at $s = 0$ in the s-domain where the high gain of K_0 dominates the shifted transfer functions K_2 and K_{-2}, that is $|K_0| \gg |K_2|$ and $|K_0| \gg |K_{-2}|$. An example showing the high gain of K_0 and its effect on $T_B(s)$ is visualized in Fig. 3. In R_1, $T_B(s)$ has an LTI approximation

$$T_B(s) \approx \frac{K_0}{K_0 + 2} = T(s) \text{ for } s \in R_1. \tag{37}$$

The performance of $T_B(s)$ in region R_1 is important because the input states (x_I, x_Q) are expected to be primarily composed of frequency components in R_1. While $T_B(s)$ could be specified directly, the computation of the corresponding K_0 is difficult.
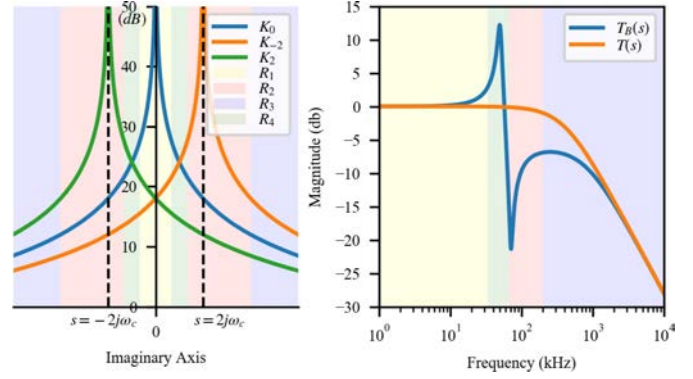

Fig. 3. For the high-gain integrator $K_0 = \frac{5e6}{s}$ (left) shows the magnitude of K_2, K_0, and K_{-2}, along with the four regions under which LTI approximations of $T_B(s)$ are derived. (right) shows the discrepancies of $T_B(s)$ from $T(s)$ in each region.

However, making the LTI approximation $T(s)$ the primary design parameter of the demodulator, the computation of K_0 is trivial.

The example in Fig. 3 shows three additional regions in the s-domain over which the characteristics of $T_B(s)$ need to be considered during design. The region R_2, centered at $s = -2j\omega_c$ is dominated by K_2 and is characterized by $|K_2| \gg |K_0|$ and $|K_0| \gg |K_{-2}|$. With this characterization $T_B(s)$ has an LTI approximation

$$T_B(s) \approx \frac{K_0(s)}{2(K_0(s) + 2)} = \frac{1}{2}T(s) \text{ for } s \in R_2 \tag{38}$$

which shows a reduction of 6 dB in the magnitude response in this region. The same expression is derived for the region around $s = 2j\omega_c$. For region R_3, for s far from $-j\omega_c$, 0, and $j\omega_c$, the transfer functions K_{-2}, K_0, and K_2 converge toward the same value. Here, the LTI approximation of $T_B(s)$ is

$$T_B(s) \approx \frac{K_0}{2K_0 + 2} \text{ for } s \in R_3. \tag{39}$$

For large K_0, the R_3 LTI approximation has 6-dB attenuation compared with $T(s)$ and approaches $T(s)$ as the K_0 becomes small. LTI approximations in R_2 and R_3 do not significantly diverge from $T(s)$.

The final region R_4, centered at $s = -j\omega_c$, is where the transfer functions K_0 and K_2 have a similar magnitude. $T_B(s)$ can diverge from the LTI approximation $T(s)$ depending on K_0, as shown in the example in Fig. 3 which shows peaking occurring in $T_B(s)$ in R_4. When K_0 has significant gain at $s = -j\omega_c$ (and equivalently at $s = j\omega_c$), $T_B(s)$ should be evaluated at $s = -j\omega_c$ to ensure that it does not excessively diverge from the nominal transfer function $T(s)$.

B. Suppression of the Cross-Coupling and Image Signals

The IQ cross-coupling describes the transfer of energy from $y_Q \longrightarrow x_I$ and $y_I \longrightarrow x_Q$ with no frequency shift. Cross-coupling results in an error in the estimated states. The transfer
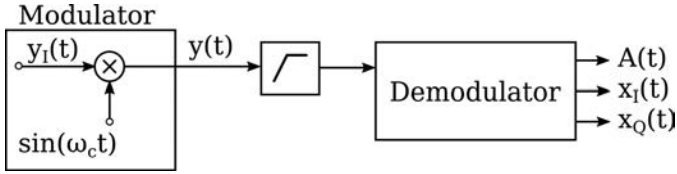
Fig. 4. Block diagram of the experimental setup. The input in-phase state $y_I(t)$ is modulated then demodulated resulting in the amplitude estimate $A(t)$, and estimated states $x_I(t)$ and $x_Q(t)$. A high-pass filter removes dc offsets introduced in the analog electronics.

function describing the cross coupling is $T_C(s)$ from (35)

$$T_C(s) = \frac{jK_0(K_{-2} - K_2)}{2(K_0 + K_{-2} + 2)(K_0 + K_2 + 2)}. \tag{40}$$

As the magnitude of K_0 is increased, the magnitude response of the cross-coupling transfer function goes to zero, that is, $|T_C(s)| \longrightarrow 0$ as $|K_0| \longrightarrow \infty$. Thus, in frequency bands where $K(s)$ has a high gain, the cross coupling is suppressed.

The same effect occurs for the image signals that are the distortions appearing in the output of the demodulator due to the mixing-induced frequency shifting. The two transfer functions from (33) and (36) which describe the mapping from the input states to the image signals are

$$T_A(s) = \frac{K_2}{2(K_2 + K_0 + 2)} \tag{41}$$

$$T_D(s) = \frac{K_{-2}}{2(K_{-2} + K_0 + 2)}. \tag{42}$$

As the magnitude of K_0 is increased, the magnitude of the up- and downconverting transfer functions tend to zero, that is, $|T_A(s)| \longrightarrow 0$ as $|K_0| \longrightarrow \infty$, and $|T_D(s)| \longrightarrow 0$ as $|K_0| \longrightarrow \infty$. Thus, in frequency bands where $K(s)$ has a high gain, the image signals are suppressed.

The Lyapunov design [18] and the Kalman filter design [16] are realized with an integrator

$$K(s) = \frac{k_i}{s}. \tag{43}$$

This filter has infinite gain at zero frequency, resulting in the complete suppression of the image signal in the estimated outputs for constant input states y_I and y_Q.

V. EXPERIMENTAL RESULTS

The experimental setup is shown in Fig. 4. The demodulator is implemented on a Xilinx Kintex-7 FPGA and analog IO is performed with the 4DSP FMC151 analog card at 122.88 MSPS. A modulator is used to generate the input signal $y(t)$ using only an in-phase signal $y_I(t)$ and zero input quadrature state. With zero input quadrature state, a nonzero quadrature estimate is used to identify cross coupling.

A. Nominal Versus Experimental Performance

A set of demodulators are designed to demonstrate the ability of the proposed design method to obtain arbitrary bandwidth

and off-mode rejection. In all cases the carrier frequency is set to 50 kHz. To demonstrate selection of off-mode rejection, four demodulators are designed with $T(s)$ specified as a Butterworth filter with fixed bandwidth of 25 kHz from first order to fourth order. To demonstrate selection of bandwidth, four demodulators are designed with $T(s)$ specified as a second-order Butterworth filter with varying bandwidths of 5, 10, 25, and 50 kHz.

For each of the designed demodulators, the direct-coupling response from $y_I(t)$ to $A(t)$ is characterized by frequency response functions (FRFs), as shown in Fig. 5(a) and (b), and step responses, as shown in Fig. 5(c) and (d). Fig. 5(a) demonstrates that the rate of attenuation in the experimental response matches the order of $T(s)$. Fig. 5(b) shows an accurate bandwidth specification for the 5, 10, and 25 kHz demodulator. For the 50-kHz demodulator, peaking is observed at the carrier frequency.

The discrepancy between the nominal and experimental responses occur for frequency components at the carrier frequency (50 kHz) and at twice the carrier frequency (100 kHz). The discrepancies between the nominal and experimental responses are greatest for the lower order and higher bandwidth $T(s)$. In addition, the image signal is clearly observed in the transient response of the first-order filter in Fig. 5(c). This indicates that greater attenuation at the carrier frequency and twice the carrier frequency corresponds to a close match between the demodulator response and LTI approximation.

B. Estimation of the Direct- and Cross-Coupling FRFs

The second-order 50-kHz Butterworth demodulator has the greatest discrepancies between the nominal and experimental FRF. The expected transfer function from $Y_I(s)$ to $X_I(s)$ is the direct-coupling transfer function $T_B(s)$ from (34). Despite a zero input quadrature state, a quadrature estimate is expected due to the cross-coupling transfer function $T_C(s)$ from (35). Fig. 6 shows the experimentally measured FRFs from y_I to the estimated in-phase x_I and quadrature x_Q states. The expected FRFs from the transfer functions in (34) and (35) match the experimental results at all frequencies except for the notches present near the carrier frequency.

The presence of these notches occurs during experimental characterization of the FRF due to the presence of an image signal. When the frequency of the input tone y_I is set to the carrier frequency ω_c, an image signal with frequency ω_c is present in the estimated states. To quantify this effect, the up- and downconverting transfer functions $T_A(s)$ and $T_D(s)$ must be considered. The magnitude of the FRFs at the carrier frequency are denoted (A_I, A_Q) and are evaluated as follows:

$$A_I = |T_B(j\omega_c) - T_A(-j\omega_c)| \tag{44}$$

$$A_Q = |-T_C(j\omega_c) - jT_A(-j\omega_c)|. \tag{45}$$

The expected and experimental A_I and A_Q at the carrier frequency 50 kHz are noted in Fig. 6. Note that the minimum value of the notches do not lie at 50 kHz. Characterization of the entire notch requires analysis to include the frequency responses of the filters within the lock-in amplifier.
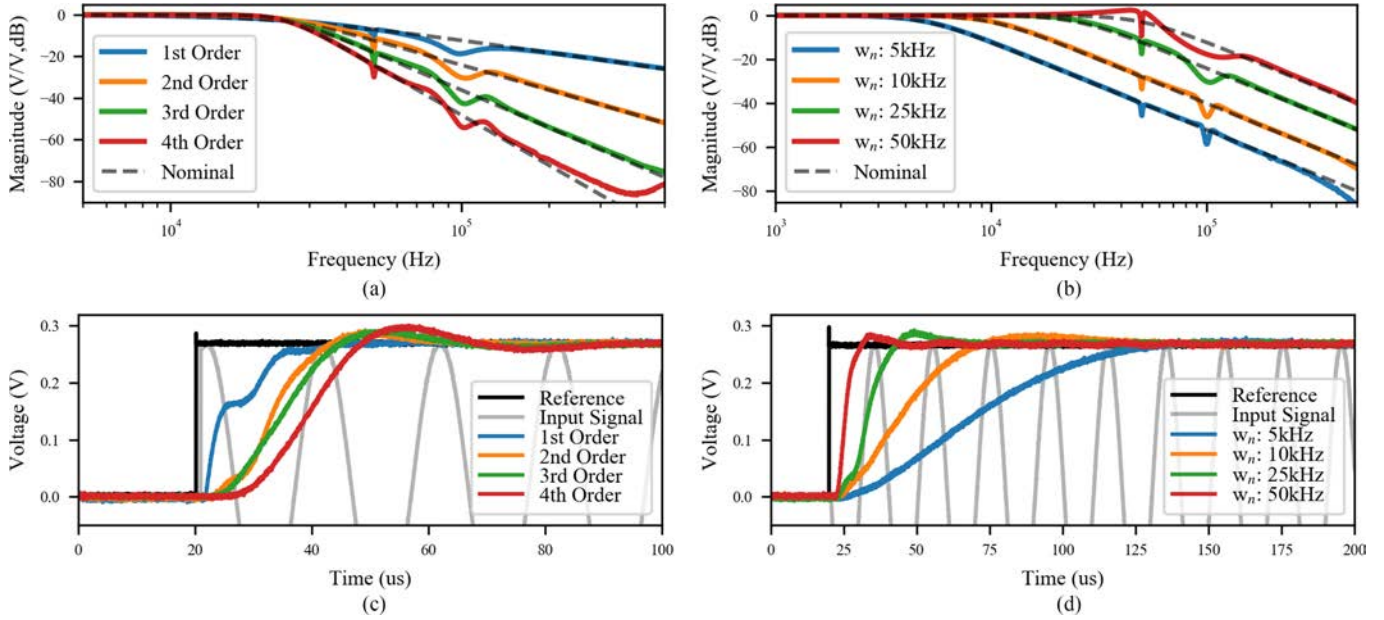
Fig. 5. Arbitrary selection of bandwidth and off-mode rejection is demonstrated with the shown set of amplitude FRFs and step responses. The nominal response is that of the specified LTI complementary sensitivity function $T(s)$. (a) FRF: 25-kHz Butterworth with varying orders. (b) FRF: second-order Butterworth with varying bandwidth. (c) Step: 25-kHz Butterworth with varying orders. (d) Step: second-order Butterworth with varying bandwidth.
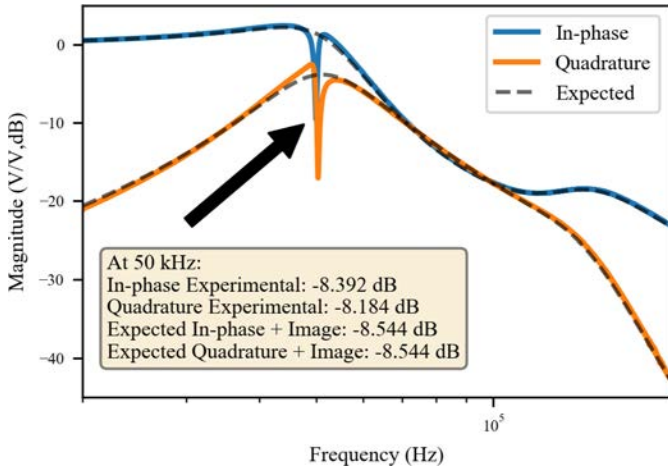

Fig. 6. Experimentally measured FRF from the input in-phase state y_I to the estimated in-phase x_I and quadrature y_Q states. The nominal transfer function is a second-order 50-kHz Butterworth filter. The expected frequency response is overlayed and the expected values at the carrier frequency are annotated.

Fig. 7. FFT of the estimated states and amplitude with y_I set to a 350 mV 10 kHz sinusoid. The nominal transfer function is a 25 kHz, 2nd Butterworth filter. The estimate at 10 kHz and the image signals at 90 and 110 kHz are the dominant components.

C. Estimation of the Image Signals

To compare the expected and experimentally observed image signals, the input state y_I to the system in Fig. 4 is set to a 10 kHz, 350 mV sinusoid and the demodulator is designed with a nominal LTI response of a second-order 25-kHz Butterworth filter. The double-sided FFT of the estimated amplitude, and estimated states are shown in Fig. 7 in which the estimate and image signals are clearly observed. The magnitude of these signals are listed in Table I.
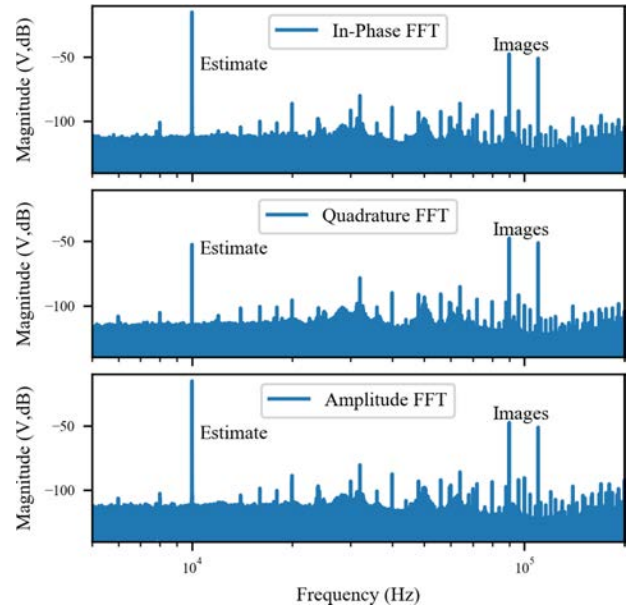
At the input frequency ω_0, the expected magnitude of both $Y_I(j\omega_0)$ and $Y_I(-j\omega_0)$ are -15.11 dB. The expected values of the estimates are

$$X_I(j\omega_0) = T_B(j\omega_0)Y_I(j\omega_0) \qquad (46)$$

$$X_Q(j\omega_0) = -T_C(j\omega_0)Y_I(j\omega_0). \qquad (47)$$

TABLE I
ESTIMATED STATES, AMPLITUDE, AND IMAGE SIGNALS WITH 10 kHz
350 mV SINUSOIDAL EXCITATION

	Expected (V, dB)	Experimental (V, dB)
In-phase		
Estimate at $10\,\mathrm{kHz}$	-15.11	-15.18
Image at $90\,\mathrm{kHz}$	-48.50	-47.65
Image at $110\,\mathrm{kHz}$	-52.03	-51.04
Quadrature		
Estimate at $10\,\mathrm{kHz}$	-52.50	-52.40
Image at $90\,\mathrm{kHz}$	-48.50	-47.56
Image at $110\,\mathrm{kHz}$	-52.03	-51.16
Amplitude		
Estimate at $10\,\mathrm{kHz}$	-15.11	-15.17
Image at $90\,\mathrm{kHz}$	-48.50	-47.54
Image at $110\,\mathrm{kHz}$	-52.03	-51.14

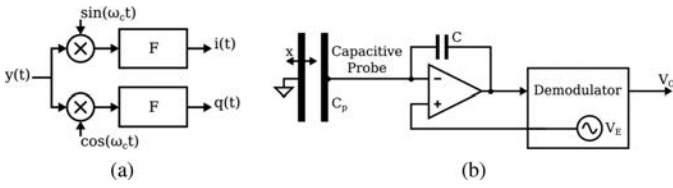The nominal transfer function is a 25 kHz, second Butterworth filter.

Fig. 8. (a) Lock-in amplifier mixes the input signal $y(t)$ with a sine and cosine signal. The system F filters the resulting product to suppress the distortion to produce the in-phase and quadrature estimate $(i(t), q(t))$. (b) Capacitive sensor setup.

The image signal at 90 kHz results from the negative frequency $(-\omega_0)$ component of the input in-phase state being upconverted

$$X_I(j(2\omega_c - \omega_0)) = -T_A(-j\omega_0)Y_I(-j\omega_0) \qquad (48)$$

$$X_Q(j(2\omega_c - \omega_0)) = -jT_A(-j\omega_0)Y_I(-j\omega_0). \qquad (49)$$

The image signal at 110 kHz results from the positive frequency (ω_0) component of the input in-phase state being upconverted

$$X_I(j(2\omega_c + \omega_0)) = -T_A(j\omega_0)Y_I(j\omega_0) \qquad (50)$$

$$X_Q(j(2\omega_c + \omega_0)) = -jT_A(j\omega_0)Y_I(j\omega_0). \qquad (51)$$

The expected and experimental magnitudes for the in-phase and quadrature signals closely match. This validates the modeling and analysis used in (46) and (51). The amplitude image signals are evaluated numerically using (6).

VI. CAPACITIVE SENSING APPLICATION

In this section, a capacitive sensing application for the proposed demodulator is examined. In addition, experiments are performed with a lock-in amplifier [see Fig. 8(a)], which is considered to be the industry standard for sensor demodulation. Like the proposed demodulator, the lock-in amplifier is implemented on a Xilinx Kintex-7 FPGA.

The architecture of the capacitive sensor is shown in Fig. 8(b). A capacitive structure is formed from a capacitive probe (Microsense 2804) and a metal target. The metal target is fixed to a nanopositioner (PI P-733.3DD) allowing its displacement
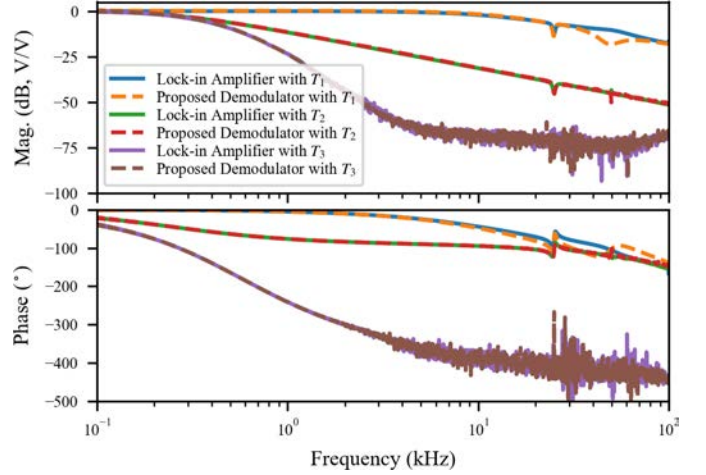

Fig. 9. Frequency response functions of the three characteristic systems realized using the lock-in amplifier architecture and proposed demodulator architecture.

x, and thus its capacitance, to be varied. A charge amplifier with a 0.5 pF reference capacitor C measures the charge flowing into the capacitive probe C_p. The charge measurement is demodulated to derive the sensor output. The characteristic equation of the capacitive sensor is

$$V_o = V_e \frac{C + C_p}{C} \qquad (52)$$

where V_o is the amplitude estimate from the demodulator, and V_e is the amplitude of the capacitive sensor 25 kHz excitation.

The performance of three demodulator specifications are considered. The nominal system T_1 is a 250-Hz fourth-order system, T_2 is a 250-Hz first-order system, and T_3 is a 12.5-kHz first-order system. The transfer functions of the nominal systems are

$$T_1(s) = \frac{1}{(2.7641 \times 10^{-04}s + 1)^4} \qquad (53)$$

$$T_2(s) = \frac{1}{(6.3662 \times 10^{-04}s + 1)} \qquad (54)$$

$$T_3(s) = \frac{1}{(1.2732 \times 10^{-05}s + 1)}. \qquad (55)$$

The first-order responses of T_2 and T_3 can be realized with Lyapunov and Kalman filter based demodulators. However, the Kalman filter implementation is computationally complex due to the Kalman gain update step which requires a matrix inversion. Both filters are inherently fixed to first order and a selected tracking bandwidth is found by empirically tuning a gain variable. In contrast, the proposed method provides a direct design approach allowing for higher order responses and selection of bandwidth without tuning.

Compared to the lock-in amplifier, the proposed demodulator is more complex due to its feedback architecture and additional multipliers, but significantly reduces the distortion of high bandwidth and low order designs. Fig. 9 shows the experimentally
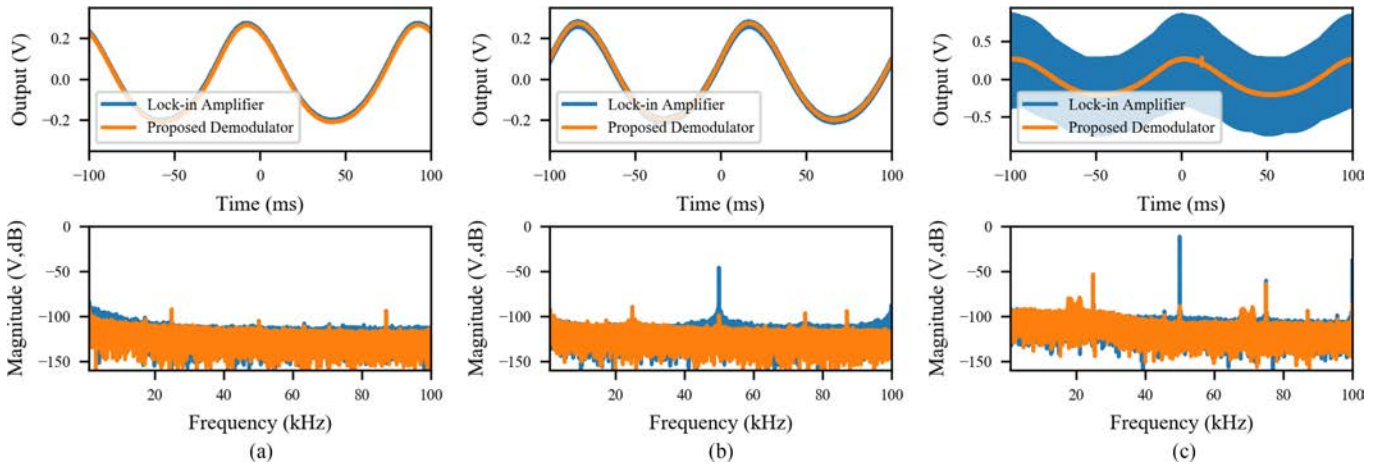
Fig. 10.   Output of the capacitive sensor (time domain and FFT) while the capacitance is varied at 10 Hz. There are six output signals for permutations of the two demodulator architectures and the three characteristic systems T_1, T_2, and T_3. (a) T_1 (250 Hz 4th Order). (b) T_2 (250 Hz 1st Order). (c) T_3 (12.5 kHz 1st Order).

TABLE II
IMAGE SIGNAL AT 50 KHZ IN THE OUTPUT SIGNAL OF THE CAPACITIVE
SENSOR FROM FIG. 10

Bandwidth (Hz)	Order	Lock-in Amplifier Image Signal (mV)	Proposed Demodulator Image Signal (mV)
250	4th	0.00219	0.00135
250	1st	10.3	0.00210
12500	1st	513	0.0775

measured FRFs of these systems implemented with both the lock-in amplifier and proposed demodulator architecture. The results show that the dynamics of both demodulator architectures match closely.

With sinusoidal motion induced in the metal target, Fig. 10(a)–(c) shows the output voltage of the capacitive sensor along with its FFT for all demodulators and Table II lists the magnitude of the image signal at 50 kHz. The 250-Hz fourth-order system performs aggressive filtering and there is no observed difference between demodulator architectures. However, as the order is reduced and/or the bandwidth is increased, the magnitude of distortion in the output signal increases. The distortion is particularly prominent in the lock-in amplifier architecture. In the 12.5-kHz first-order system, an image signal at 50 kHz has a magnitude of 513 mV. This image signal is suppressed in the proposed demodulator architecture. The harmonic components at 25 and 75 kHz in both architectures are due to nonlinearities in the capacitive sensor instrumentation, and harmonics that exist in the excitation voltage.

The performance benefits of the proposed demodulator compared to a lock-in amplifier are observed when applying feedback control using a capacitive sensor, as shown in Fig. 11(a). The closed-loop step responses of this system are shown in Fig. 11(b). The fourth-order demodulators heavily suppress the image signal but erode stability margins due to their additional phase lag compared to the first-order demodulators,
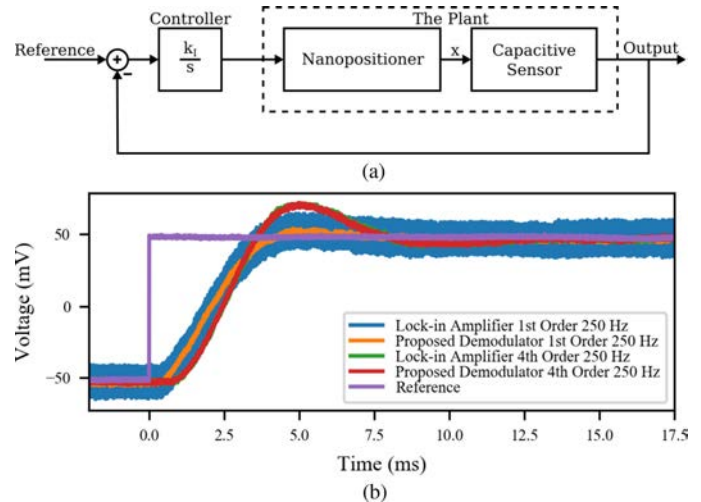

Fig. 11.   (a) Block diagram of the system in feedback, $k_I = 7000$. (b) Step responses of the closed-loop system using different demodulator architectures, and characteristic systems.

as observed with their additional overshoot. However, with the less aggressive filtering of the low-order demodulators, the image signal distorts the sensor output when using the lock-in amplifier architecture. This distortion is absent using the proposed demodulator.

VII. CONCLUSION

This paper outlines a demodulator architecture with improved image rejection compared to lock-in amplifiers. The absence of the image signal permits greater bandwidth and the use of low-order dynamics. The dynamics of the proposed linear time periodic system are modeled, from which an LTI approximation is formed, which facilitates the use of linear control design methods to synthesize the demodulator.

The experimental results demonstrate the ability to arbitrarily tune both the bandwidth and off-mode rejection of the demodulator, which cannot be achieved with previously reported high-speed demodulators, such as the Kalman filter and Lyapunov filter based demodulators. Experimental results verify the derived frequency responses and presence of distortion in the estimated states.

The proposed demodulator architecture provides a greater degree of design flexibility which allows the response to be tailored to the specific requirements of an application. As such, this eliminates the demodulation process as a constraint on system design and performance.

REFERENCES

[1] V. Kaajakari, *Practical MEMS*. Las Vegas, USA: Small Gear Publishing, 2009.
[2] A. Mohammadi, M. Yuce, and S. O. Reza Moheimani, "A low-flicker-noise MEMS electrothermal displacement sensing technique," *J. Microelectromech. Syst.*, vol. 21, no. 6, pp. 1279–1281, 2012.
[3] W. Yang, "Design of electrical capacitance tomography sensors," *Meas. Sci. Technol.*, vol. 21, no. 4, 2010, Art. no. 042001.
[4] M. B. Coskun, K. Thotahewa, Y.-S. Ying, M. Yuce, A. Neild, and T. Alan, "Nanoscale displacement sensing using microfabricated variable-inductance planar coils," *Appl. Phys. Lett.*, vol. 103, no. 14, 2013, Art. no. 143501.
[5] J. Fraden, *Handbook of Modern Sensors: Physics, Designs, and Applications*. New York, NY, USA: Springer, 2010.
[6] A. J. Fleming, "A review of nanometer resolution position sensors: Operation and performance," *Sensors Actuators A, Phys.*, vol. 190, no. 1, pp. 106–126, 2013.
[7] L. K. Baxter, *Capacitive Sensors: Design and Application*. Piscataway, NJ, USA: IEEE Press, 1997.
[8] R. García and R. Pérez, "Dynamic atomic force microscopy methods," *Surf. Sci. Rep.*, vol. 47, no. 6-8, pp. 197–301, 2002.
[9] W. C. Michels and N. L. Curtis, "A pentode lock-in amplifier of high frequency selectivity," *Rev. Sci. Instrum.*, vol. 12, no. 9, pp. 444–447, 1941.
[10] M. G. Ruppert, D. M. Harcombe, M. R. P. Ragazzon, S. O. Reza Moheimani, and A. J. Fleming, "A review of demodulation techniques for amplitude modulation atomic force microscopy," *Bellstein J. Nanotechnol.*, vol. 8, pp. 1407–1426, 2017.
[11] T. Ando, N. Kodera, E. Takai, D. Maruyama, K. Saito, and A. Toda, "A high-speed atomic force microscope for studying biological macromolecules," *Proc. Nat. Acad. Sci.*, vol. 98, no. 22, pp. 12468–12472, 2001.
[12] T. Uchihashi, T. Ando, and H. Yamashita, "Fast phase imaging in liquids using a rapid scan atomic force microscope," *Appl. Phys. Lett.*, vol. 89, no. 21, 2006, Art. no. 213112.
[13] J. Kokavecz, Z. Tóth, Z. L. Horváth, P. Heszler, and A. Mechler, "Novel amplitude and frequency demodulation algorithm for a virtual dynamic atomic force microscope," *Nanotechnology*, vol. 17, no. 7, pp. S173–S177, 2006.
[14] D. Y. Abramovitch, "Low latency demodulation for atomic force microscopes, Part I efficient real-time integration," in *Proc. Amer. Control Conf.*, 2011, pp. 2252–2257.
[15] K. S. Karvinen and S. O. Reza Moheimani, "A high-bandwidth amplitude estimation technique for dynamic mode atomic force microscopy," *Rev. Sci. Instrum.*, vol. 85, no. 2, 2014, Art. no. 023707.
[16] M. G. Ruppert, K. S. Karvinen, S. L. Wiggins, and S. O. Reza Moheimani, "A Kalman filter for amplitude estimation in high-speed dynamic mode atomic force microscopy," *IEEE Trans. Control Syst. Technol.*, vol. 24, no. 1, pp. 276–284, Jan. 2016.
[17] M. G. Ruppert, D. M. Harcombe, and S. O. Reza Moheimani, "High-bandwidth demodulation in MF-AFM: A Kalman filtering approach," *IEEE/ASME Trans. Mechatronics*, vol. 21, no. 6, pp. 2705–2715, Dec. 2016.
[18] M. R. P. Ragazzon, M. G. Ruppert, D. M. Harcombe, A. J. Fleming, and J. T. Gravdahl, "Lyapunov estimator for high-speed demodulation in dynamic mode atomic force microscopy," *IEEE Trans. Control Syst. Technol.*, vol. 26, no. 2, pp. 765–772, Mar. 2018.
[19] D. M. Harcombe, M. G. Ruppert, M. R. P. Ragazzon, and A. J. Fleming, "Lyapunov estimation for high-speed demodulation in multifrequency atomic force microscopy," *Beilstein J. Nanotechnol.*, vol. 9, pp. 490–498, 2018.
[20] M. G. Ruppert, D. M. Harcombe, S. I. Moore, and A. J. Fleming, "Direct design of closed-loop demodulators for amplitude modulation atomic force microscopy," in *Proc. Annu. Amer. Control Conf.*, Milwaukee, WI, USA, 2018, pp. 4336–4341.
[21] R. G. Lyons, *Understanding Digital Signal Processing*. Englewood Cliffs, NJ, USA: Prentice-Hall, 2010.

Steven Ian Moore received the bachelor's degree in electrical engineering and the bachelor's degree in mathematics from The University of Newcastle, Callaghan, NSW, Australia, in 2012, and the Ph.D. degree in electrical engineering from The University of Newcastle, Australia, in 2016.

He is currently a Postdoctoral Researcher with the Precision Mechatronics Lab, The University of Newcastle. His research focus is on the design, modeling, implementation, and optimization of mechatronic systems including precision motion control and sensing in microelectromechanical systems (MEMS), structural design of piezoelectric microcantilevers, nanopositioning, ultrahigh bandwidth fixed point control realizations, image stabilization in optical systems, and inertial stabilization systems.

Michael G. Ruppert (M'14) received the Dipl.-Ing. degree in automation technology in production from the University of Stuttgart, Stuttgart, Germany, in 2013, and the Ph.D. degree in electrical engineering from The University of Newcastle, Callaghan, NSW, Australia, in 2017.

He was a Visiting Researcher with The University of Texas at Dallas, USA from 2015 to 2016. He is currently a Postdoctoral Research Fellow with The University of Newcastle. His research interests include the utilization of system theoretic tools for sensing, estimation and control in high-speed and multifrequency atomic force microscopy.

Dr. Ruppert's research has been recognized with the 2018 IEEE Transactions on Control Systems Technology Outstanding Paper Award, the 2017 University of Newcastle Higher Degree by Research Excellence Award and Best Conference Paper Finalist Awards at the 2018 International Conference on Manipulation, Automation and Robotics at Small Scales (MARSS), and the 2013 IEEE/ASME International Conference on Advanced Intelligent Mechatronics (AIM).

David M. Harcombe received the Bachelor of Engineering degree (first class Hons.) in electrical from The University of Newcastle, Callaghan, NSW, Australia, with the University Medal, in 2016. He is currently working toward the Ph.D. degree at the Precision Mechatronics Lab, School of Electrical Engineering and Computing, The University of Newcastle.

His research areas include high-speed signal processing and control in AFM as well as the design of a piezoelectric cantilever gas sensor.
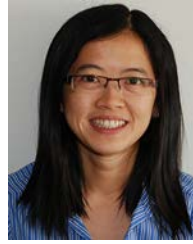
Andrew J. Fleming (M'02) received the Bachelor of Electrical Engineering and Ph.D. degrees in electrical engineering from The University of Newcastle, Callaghan, NSW, Australia (Callaghan campus), in 2000 and 2004, respectively.

He is the Director of the Precision Mechatronics Lab, The University of Newcastle, Australia. His research interests include lithography, nanopositioning, scanning probe microscopy, and biomedical devices. He is the coauthor of three books and more than 180 journal and conference articles.

Dr. Fleming's research awards include the ATSE Baterham Medal in 2016, the IEEE Control Systems Society Outstanding Paper Award in 2007, and The University of Newcastle Researcher of the Year Award in 2007. He holds several patent applications, and in 2012 he received the Newcastle Innovation Rising Star Award for Excellence in Industrial Engagement.

Yuen Kuan Yong (M'09) received the Bachelor of Engineering degree in mechatronics engineering and the Ph.D. degree in mechanical engineering from The University of Adelaide, Adelaide, SA, Australia, in 2001 and 2007, respectively.

She is currently an Associate Professor with the School of Electrical Engineering and Computing, The University of Newcastle, Callaghan, NSW, Australia. Her research interests include nanopositioning systems, design and control of novel microcantilevers, atomic force microscopy, and miniature robotics.

Dr. Yong was the recipient of the University of Newcastle Vice-Chancellors Award for Research Excellence in 2014, and the Vice-Chancellors Award for Research Supervision Excellence in 2017. She was an Australian Research Council DECRA Fellow from 2013 to 2017. She is an Associate Editor for the IEEE/ASME TRANSACTIONS OF MECHATRONICS.